Optical fiber-based photocathode: Supplemental Information

Albert Căsăndruc, Robert Bücker, Günther Kassier, and R. J. Dwayne Miller

Slit scan electron optics

Initial electron distribution The lateral position x, y and emission angle $\theta_\mathrm{x}, \theta_\mathrm{y}$ of each electron emitted from the cathode are drawn from a phase space distribution $W(x, y, \theta_\mathrm{x}, \theta_\mathrm{y}; z = 0)$. In the following, we assume that: 1. emission behaves homogeneously and linearly, i.e. the angular emission pattern is neither dependent on position, nor on laser intensity; 2. the cathode surface is flat.[1] It is then valid to factorize the phase space distribution as

$$W(x, y, \theta_\mathrm{x}, \theta_\mathrm{y}; z = 0) \approx N(x, y) \cdot G(\theta_x, \theta_y), \tag{S1}$$

where $N(x, y)$ is the spatial distribution of electron emission on the cathode, and $G(\theta_x, \theta_y)$ the local angular distribution.

To analyze results of the slit scan along x, it is sufficient to consider the one-dimensional projections of the distribution functions $n(x) \equiv \int N(x, y)\mathrm{d}y$ and $g(\theta) \equiv \int G(\theta = \theta_\mathrm{x}, \theta_\mathrm{y})\mathrm{d}\theta_\mathrm{y}$. For the angular emission pattern we can reasonably assume a thermal (Gaussian) distribution $g(\theta) \propto \exp(-\theta^2/2\sigma_\theta^2)$ with an RMS radius σ_θ. The spatial distribution $n(x)$ depends strongly on the particular shape of both the cathode and the excitation light. For data analysis we assumed two different test functions, namely, a Gaussian distribution $n_\mathrm{G}(x) = (2\pi\sigma_x^2)^{-1/2} \exp(-x^2/2\sigma_x^2)$ with RMS radius σ_x, and the one-dimensional projection of a homogeneous circle with radius R: $n_\mathrm{c}(x) = (2/\pi r)\sqrt{1 - (x/r)^2}$, yielding an RMS radius of $r/2$.

Acceleration Typically, after emission, electrons are directly accelerated away from the cathode to their final kinetic energy reached at an anode, resulting in a reduction of all trajectory angles. For a flat cathode it is easy to show that in terms of the electron distribution at the anode this is equivalent to an effective doubling of the propagation length between cathode and anode; in the following we will hence always refer to a *virtual* cathode, that is displaced accordingly along the optical axis, but otherwise unchanged.

[1] The case of curved cathodes, where a linear correlation between position and angle (chirp) is present already at the cathode can be readily taken into account by deriving a non-chirped *virtual source*, which would yield the same electron distribution at the cathode position, but has a different (virtual) size and position than the physical cathode.

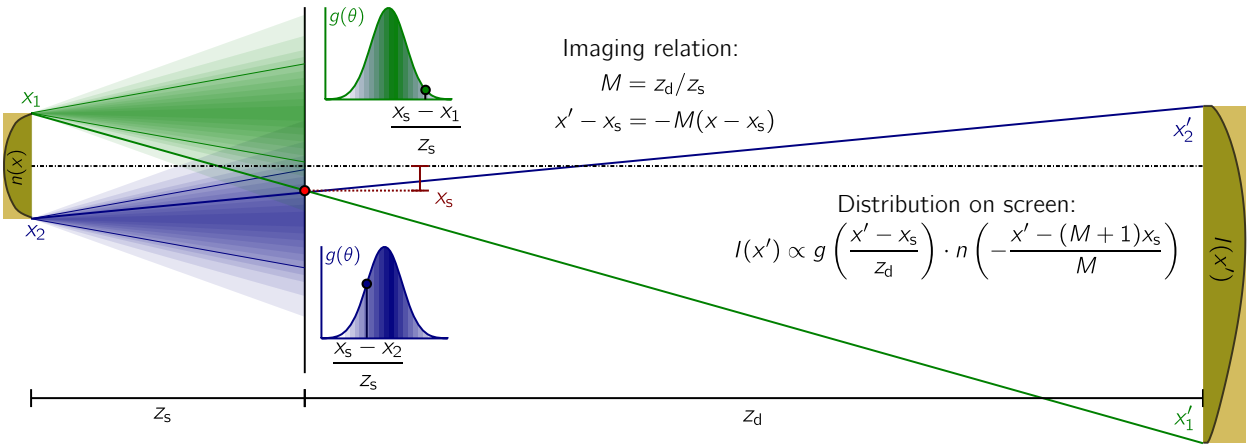

FIG. S1: Ray optical construction for imaging of an electron source with distribution functions $n(x), g(\theta)$ through a slit placed at position z_s, x_s, shown as red dot. See main text for detailed explanation.

Propagation through slit To compute the density profile along x of electrons hitting the detector after having passed the slit at position z_s, we can propagate the initial phase space distribution to the screen using the propagation law $w(x, \theta; z_s) = w(x - \theta z_s, \theta; 0)$, remove parts of the distribution outside the slit, and propagate similarly to the screen. The same result can be obtained in a more instructive way using a ray optical construction as shown in fig. S1. Electrons are launched from a (virtual, see above) cathode at $z = 0$ with a spatial distribution $n(x)$ and an angular distribution $g(\theta)$. Ray bundles emitted from two positions x_1, x_2 near the edges of the cathode are shown in green and blue shading, respectively. Assuming an infinitely narrow slit, for each position x along the cathode, exactly one ray can pass the slit at an angle $\theta = (x_s - x)/z_s$ (bold green and blue lines), where x_s denotes the lateral position of the slit. These rays hit the detector placed after a distance z_d at positions x', respectively, and form a pinhole image of the cathode. It can be readily concluded from the ray diagram that the initial and final position of the transmitted rays are related as $(x' - x_s) = -M(x - x_s)$, where the magnification M is given by $M = z_d/z_s$. Finally, we have to take into account the initial angular distribution $g(\theta)$; from the angle of a ray emitted from position x through the slit it follows that its relative current is proportional to $g(\theta = (x_s - x)/z_s)$. In fig. S1, two insets are shown which depict this relation for the emission points x_1 and x_2.

The final intensity profile on the detector for a given slit position $I(x'; x_s)$ is then given by

a product of the pinhole image with the relative intensity of the rays. Solving the imaging relation given above for x, we obtain $x = -M^{-1}(x' - (M+1)x_\mathrm{s})$, which we can insert into $n(x)$ and $g(\theta)$ to obtain:

$$\begin{aligned} I(x'; x_\mathrm{s}) &\propto g\left(\frac{x_\mathrm{s} - x}{z_\mathrm{s}}\right) n(x) \\ &= g\left(\frac{x' - x_\mathrm{s}}{z_\mathrm{d}}\right) n\left(-\frac{x' - (M+1)x_\mathrm{s}}{M}\right). \end{aligned} \tag{S2}$$

Notably, each of the peaked functions g and n is shifted by a different amount if $x_\mathrm{s} \neq 0$, which generally results in a skew peak shape, as indicated in fig. S1.

Analysis of experimental data

Each of the slit scan measurements as described in the text provides us with profiles $I(x'; x_\mathrm{s})$ for a set of typically 10-20 values of x_s. We analyze the data in several steps:

- The beam profile at the slit is obtained by integrating over x': $I_\mathrm{s}(x_\mathrm{s}) = \int I(x'; x_\mathrm{s})\mathrm{d}x'$. These profiles are shown in panel (b) of fig. 3 in the main text and supplemental figures S2 and S3 below. We find that for all data sets, a Gaussian distribution describes the data fairly well, indicating that the slit is placed sufficiently in the far field of the (virtual) source, such that the shape of the initial spatial distribution becomes irrelevant.

- If the measured values of x_s are sufficiently dense, by numerically integrating over x_s we obtain an estimate of the *total* beam profile on the screen, which would be found in the absence of the slit: $I_\mathrm{t}(x') = \int I(x'; x_\mathrm{s})\mathrm{d}x'$. As the detector is located in the far field of the emitter, we expect that it is defined by the initial momentum distribution: $I_\mathrm{t}(x') \propto g(x'/(z_\mathrm{d} + z_\mathrm{s}))$. Formally this arises from eq. S2 if assuming that the contributions of g and n have similar peak widths in their argument (or n more narrow), which is fulfilled in our data. The dependence of $I(x'; x_\mathrm{s})$ on x_s is then almost entirely contained in $n(\ldots)$, as $M \gg 1$, and we can approximate the factor

$n(\ldots)$ in above integration by a delta function:

$$\begin{aligned} I_{\mathrm{t}}(x') &= \int I(x'; x_{\mathrm{s}}) \mathrm{d}x' \\ &\approx \int g\left(\frac{x_{\mathrm{s}} - x}{z_{\mathrm{s}}}\right) \delta\left(-\frac{x' - (M+1)x_{\mathrm{s}}}{M}\right) \mathrm{d}x' \\ &= \left(\frac{M}{M+1}\right) g\left(\frac{x'}{z_{\mathrm{d}} + z_{\mathrm{s}}}\right), \end{aligned}$$

where the prefactor is ≈ 1. We find that $I_{\mathrm{t}}(x')$ can be fitted very accurately by a Gaussian distribution. Through this analysis, we obtain a good estimation for the angular distribution $g(\theta)$ directly from our data.

- We now fit the expression for $I(x'; x_{\mathrm{s}})$ given in eq. S2 to the profiles for each x_{s}, using a fixed Gaussian function $g(\theta)$ as obtained in the previous step, and test functions for a Gaussian and a homogeneous source (as described above) for $n(x)$. Besides an amplitude scaling, the fit allows for two free parameters $R = Mr$, and $c = Mx_{\mathrm{s}}$; as x_{s} is known *a priori*, values for the magnification M and source radius r can be deduced. Note, that while a single fit for *all* measured positions x_{s} with fixed r, M could have been applied, only unsatisfactory results could be obtained by such an approach, which we attribute to unaccounted experimental imperfections as will be discussed below. The fits and corresponding data points are shown in panel (a) of fig. 3 in the main text and supplemental figures S2 and S3.

- Finally, we calculate the RMS emittance of the beam from the fits of $I_{\mathrm{s}}(x_{\mathrm{s}})$ and $I(x'; x_{\mathrm{s}} \approx 0)$, by computing the RMS values of the fit lines which correspond to spatial and angular RMS widths *at the slit position* σ_{x} and σ_θ, respectively.[2] As explained in the main article, those are multiplied with each other and the normalization factor $\sqrt{p_{\mathrm{z}}/mc}$ to obtain the emittance. Inferring the beam emittance in this way does not rely on any of the assumptions concerning the optical construction outlined before. Quantitatively identical results could be obtained using any (even purely phenomenological) fit function that accurately reproduces the data, or even the data points directly, which however would lead to large uncertainties arising from noise contributions in the wings of the distributions. To estimate the uncertainty of the obtained values, 95% confidence ranges were calculated for the fit coefficients.

[2] While identical values for σ_θ should be obtained for $I(x'; x_{\mathrm{s}} \neq 0)$, this is found to not always be the case, as discussed below.

Application to data sets

We applied the procedure outlined so far to the data collected for the three experiments presented in the article. While we used the same principal data analysis, several qualitative differences were found for the data sets:

1. 50 µm *fiber diameter,* 200 V *acceleration voltage (fig. 3 in main text).* In this data set, using a circular test function for the emission profile $n \propto \sqrt{1-(x^2/r^2)}$ yields excellent agreement between the fitted curves for $I(x';x_\mathrm{s})$, as shown for several values of x_s in fig. 3a. A magnification of $M = 23$ is found, less than expected from the experiment geometry by approximately a factor of two; we ascribe this finding to an inaccurate determination of the emitter-slit distance z_s, which however does not affect the final result for the emittance ϵ. From the fits over most of the range of x_s, an emitter diameter of $r = 50\,\mu\mathrm{m}$ is consistently inferred, which drops significantly for the few outermost measured values of x_s. The additional acceleration of 80 V between slit and detector has been taken into account by increasing the effective distance between slit and detector by a factor of $2 \cdot \sqrt{280\,\mathrm{V}}/(\sqrt{200\,\mathrm{V}}+\sqrt{280\,\mathrm{V}}) \approx 1.08$.

2. 100 µm *fiber diameter,* 1500 V *acceleration voltage (supplemental figure S2).* Compared to the first data set, modifications to the setup have been made to allow for a larger acceleration voltage of V_acc =-1500 V ($p_\mathrm{z}/mc \approx 0.077$), at a distance between the photocathode and aperture of d_acc=3 mm, and for a free drift region after the slit aperture d_drift=105 mm. As opposed to the previous set, using a Gaussian test function $n \propto \exp(-x^2/2\sigma^2)$ was necessary to obtain agreement with experimental data, as seen in fig. 4a. We conjecture that this might be due to manufacturing details of the cathode, such as significant intensity in the cladding region, or a slight curvature of the emitting surface, which would lead to the virtual cathode having a different emission profile than the physical. The found magnification is $M = 20$, slightly larger than expected from experiment geometry (which, again, does not affect the main results). Also we find a much more pronounced decay of the inferred source size with more off-centered slit positions x_s, approximately linearly decreasing from a Gaussian equivalent radius of $r_\mathrm{eq} = 2\sigma = 38\,\mu\mathrm{m}$ to less than half that value near the outer edge of the momentum distribution (see peak widths in fig. S2). We suspect this to be

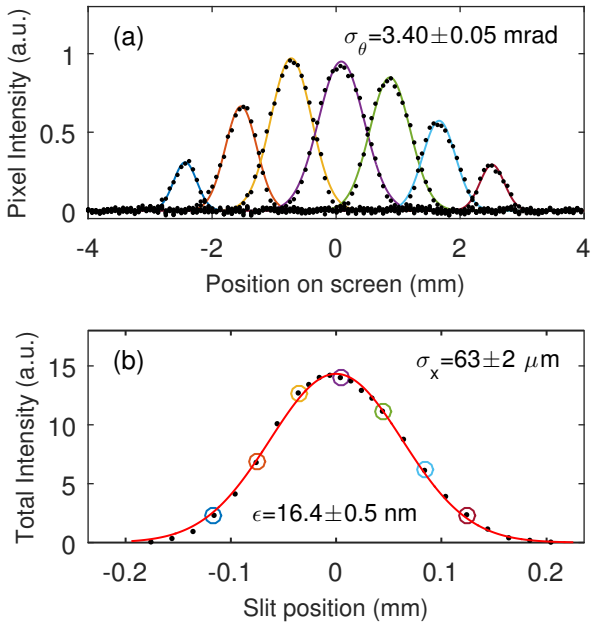

FIG. S2: Measurement results for a 100 µm core size fiber-based cathode at 1500 V acceleration voltage, as described in the main text. See fig. 3 in main text for description of the panels.

an effect of either details of the fiber tip shape, such as the emitting surface being somewhat recessed inside the cladding structure, or finite thickness of the scanning slit along the optical axis. In both cases the data taken at $x_s \approx 0$ should be accurate and hence are used for determination of emittance.

3. 100 µm *fiber diameter,* 70 kV *acceleration voltage (supplemental figure S3).* The geometry in this setup is defined by $d_{\mathrm{acc}} = 14\,\mathrm{mm}$ and $d_{\mathrm{drift}} = 592\,\mathrm{mm}$. As opposed to set 2, and similarly to set 1, the projected circular distribution for $n(x)$ worked significantly better than the Gaussian. Even though the same fiber type has been used as in set 2, besides sample-to-sample differences, the rather different manufacturing process for the high-voltage compatible cathode may readily explain this difference. In contrast to the other two sets, weak but rather wide wings were found in the intensity profiles, which we attribute to the point spread function of the fiber-coupled CCD imaging system employed in the high-voltage setup. For the fits, we take this into account by convolution with a Lorentzian profile of 1.8 µm FWHM; this consistently leads to good fits over the entire range of x_s values. The found magnification is $M = 17$. Again, we notice a strong drop-off of the imaged source size for large off-axis positions of x_s,

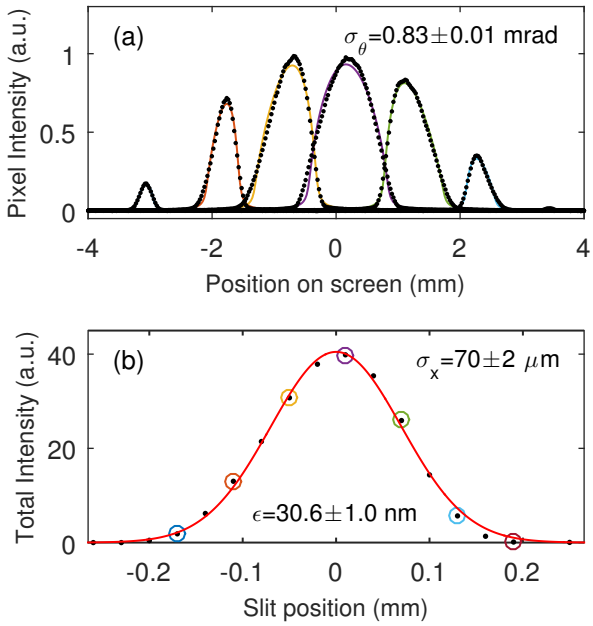

FIG. S3: Measurement results for a 100 µm core size fiber-based cathode at 70 kV acceleration voltage, as described in the main text. See fig. 3 in main text for description of the panels.

from $R = 39\,\mu\text{m}$ to approximately 20% of that value near the edges, as can be seen from the beam profiles in figure S3. Similarly as before, we argue that at $x_s \approx 0$ the factors suspected to cause the drop-off become insignificant.